Biomimetic artificial water channel membranes for enhanced desalination

Maria Di Vincenzo, Alberto Tiraferri, Valentina-Elena Musteata, Stefan Chisca, Rachid Sougrat, Li-Bo Huang, Suzana P Nunes, Mihail Barboiu

Biomimetic artificial water channels membranes for enhanced desalination

Maria Di Vincenzo,[1] Alberto Tiraferri,[2] Valentina-Elena Musteata,[3] Stefan Chisca,[3] Rachid Sougrat,[4] Li-Bo Huang,[1,5] Suzana P. Nunes,[3] Mihail Barboiu[1,5]

[1]Institut Européen des Membranes, Adaptive Supramolecular, Nanosystems Group, University of Montpellier, ENSCM, CNRS, Place Eugène Bataillon, CC 047, F-34095, Montpellier, France. [2] Department of Environment, Land and Infrastructure Engineering (DIATI), Politecnico di Torino, Corso Duca degli Abruzzi 24, 10129 Turin, Italy. [3]King Abdullah University of Science and Technology (KAUST), Biological and Environmental Science and Engineering Division, Advanced Membranes and Porous Materials Center, 23955-6900, Thuwal, SaudiArabia. [4]King Abdullah University of Science and Technology (KAUST), Core Labs, 23955-6900, Thuwal, Saudi Arabia [5]Lehn Institute of Functional Materials, School of Chemistry, Sun Yat-Sen University, Guangzhou 510275, China.

*Corresponding Author. E-mail: mihail-dumitru.barboiu@umontpellier.fr

Inspired by biological proteins, artificial water channels-AWCs can be used to overcome the performances of traditional desalination membranes. Their rational incorporation in composite polyamide, provides the first example of biomimetic membranes, applied under representative reverse osmosis desalination conditions, with intrinsically high water-to-salt permeability ratio. The hybrid polyamide presents larger voids and seamlessly incorporates I–quartet AWCs for highly selective transport of water. These biomimetic membranes can be easily scaled for industrial standards (> m^2), provide 99.5% rejection of NaCl or 91.4 % rejection of boron, with water flux of 75 L m^{-2} h^{-1} at 65 bar and 35000 ppm NaCl feed solution, representative of seawater desalination. This flux is more than 75% higher than that observed with current state-of-the-art membranes with equivalent solute rejection, translating into an equivalent reduction of the membrane area for the same water output and a ~12% reduction of the required energy for desalination.

Water scarcity is one of the important challenges of our time[1,2]. Membrane-based technologies have a tremendous role in addressing this challenge by allowing efficient water purification and desalination[3]. Desalination membranes allowing the transport of water while rejecting solutes are used in seawater reverse osmosis (SWRO) and brackish water reverse osmosis (BWRO).

Thin-film composite (TFC) polyamide (PA) membranes prepared *via* interfacial polymerization (IP), have served as standard for SWRO and BWRO during the last 40 years[4]. The control of the film morphology,[5-7] or the incorporation of nanofillers[8–10] have been shown to increase the water permeability, while generally leading to lower selectivity, as the resulting defects in the active layer affect the solute retention. To overcome the selectivity-permeance trade-off whilst keeping a water permeance of at least 2-4 L m^{-2} $h^{-1}$$bar^{-1}$[11], completely new approaches would be required.

Biological Aquaporins-AQPs[12,13], exhibiting high water permeability and total ionic rejection, have been embedded in artificial *bio-assisted membranes*. Nonetheless, there are many challenges to overcome with the goal to preserve their activity at high-salinity and high-pressure conditions, or to obtain high-density AQP-based membranes[14]. Parallel to these investigations, straightforward synthetic *biomimetic artificial water channels*-AWCs have been proposed[15,16]. The development of AWCs[17–21] have increased the prospect to use these materials in desalination technologies, since their structure can be tuned to control the water translocation in a biomimetic fashion[22], with near-perfect selectivity[23]. Flat-sheet films (> cm^2) embedding graphene, carbon nanotubes[24-26] or pillar[5]arenes[27] have led to large improvements in water permeance (20-65 L $m^{-2}h^{-1}bar^{-1}$), but their salt rejection is typically limited with little interest for seawater desalination. These results are related to important scale-up challenges in translating molecular transport to performant meter-scale membranes. We postulate that one of the creative strategies for addressing such scale-up challenges is to combine the PA material, known for its scalability *via* the integration within a typical roll-to-roll processing system, with the highly permeable and selective AWCs. The key challenge in the construction of such

hybrid material is the required adaptive gentle interaction between polyamide and water channels, preventing the formation of defects.

Herein, we report the incorporation of AWC within scalable biomimetic membranes that remarkably outperform the classical RO membranes. The novel strategy leads to a greater fundamental understanding of how AWC incorporation, starting from their colloidal self-assembled superstructures, can be optimized at the nanoscale to facilitate the selective transport of water, mainly occurring through channels. One novelty here is related to the identification of unexpected sponge-like superstructures of the hybrid PA-AWC materials. Moreover, all other selective channels or materials previously reported in literature[23–27] remain applicable in principle, while the biomimetic membranes reported here are the first materials of this type tested and applied under seawater desalination conditions with representative pressure and crossflow conditions of full-scale systems. The relatively straightforward quantification of biomimetic imidazole-quartet, I-quartet AWCs, relevant to subsequently construct RO membranes in larger scale based on such probes, is a particularly important and previously unreported strategy.

Kinetic formation of AWC-PA membranes prepared via IP.

Our fabrication strategy of AWC-PA layers is adding one preliminary step to the conventional IP[4] method (Fig. 1a): Hexylureido-ethyl-imidazole (HC6) was dissolved in a ethanolic aqueous solution, followed by sonication to obtain a colloidal AWC aggregates, that was dispersed onto the active surface of commercial polysulfone (PSf) support before starting the traditional IP procedure. During the IP, the AWCs can produce highly dispersed crystalline phases, that are probably cross-linked with growing PA oligomers into hybrid nanoparticles of 30-40 nm in diameter, integrated into the PA after a controlled aggregation / crystallization process. The morphology of the layer depends on the density of the AWCs nanoparticles interacting with the surrounding PA matrix. To improve the homogeneity the AWCs distribution, different IP protocols were investigated. In the best procedure, the AWCs

solution was left to sit on the PSf for 60 s and a 2 w/w% solution of MPD monomer was made to react with a 0.1 w/w% solution of TMC monomer during the ensuing IP; the membranes thus formed are referred to as "optimized TFC-HC6 membranes". The reference TFC membranes were prepared with the same procedure.

To gain insight into the mechanism of formation of colloidal aggregates, we monitored different samples by dynamic light scattering (DLS). When 0.2 mL of water were added to a 1-mL ethanolic solution of 0.5 % HC6, a reversible formation of aggregates (D_h =600 - 800 nm) was observed, which was followed by a re-dispersion *via* ultra-sonication for 15 min. (Supplementary Fig. 2a). Small angle X-ray scattering (SAXS) profiles provided information and confirmed that, no structures smaller than 150 nm were detected for diluted HC6 (Supplementary Fig. 3). For more concentrated solutions of 1.0-2.0 % HC6, smaller aggregates (D_h = 70 - 200 nm) were observed after adding 2-6 mL water to 1 mL HC6 ethanolic solution, without any visible precipitation (Supplementary Fig. 2b,c). Smaller aggregates (D_h = 70 nm) were obtained when a 2 w/w% aqueous solution of MPD was used instead of pure water (D_h = 200 nm), reminiscent of H-bonding between colloidal aggregates of AWC and MPD (Supplementary Table 1). Additional SAXS experiments performed on samples of 1% HC6 in 5:1 ethanol/water, upon addition of water to shift the ratio to 1:1 indicate the presence of mass-fractal structures with about 15 nm radius of gyration and Porod slope around 3 (Supplementary Table 2, Fig. 4). These conditions simulate those corresponding to the best results for the nanoaggregates formation and IP membrane preparation in this study.

To better explain the hybrid particles formation and their integration into PA, it is important to consider their nano-crystallization from water/ethanol solutions. The X-ray powder diffraction patterns of bulk crystalline powders obtained from colloidal suspensions are indicative of lamellar phases, with the main diffraction peaks at 2θ = 3.46° (*100*), 6.95° (*200*), and 8.04° (*300*), corresponding to interplanar distances of 25.4, 12.5, and 8.4 Å, respectively[20,22], and of the two minor (< 10 %) polymorphs (2θ = 3.62° or 4.09° (*100*)) (Supplementary Fig. 6).

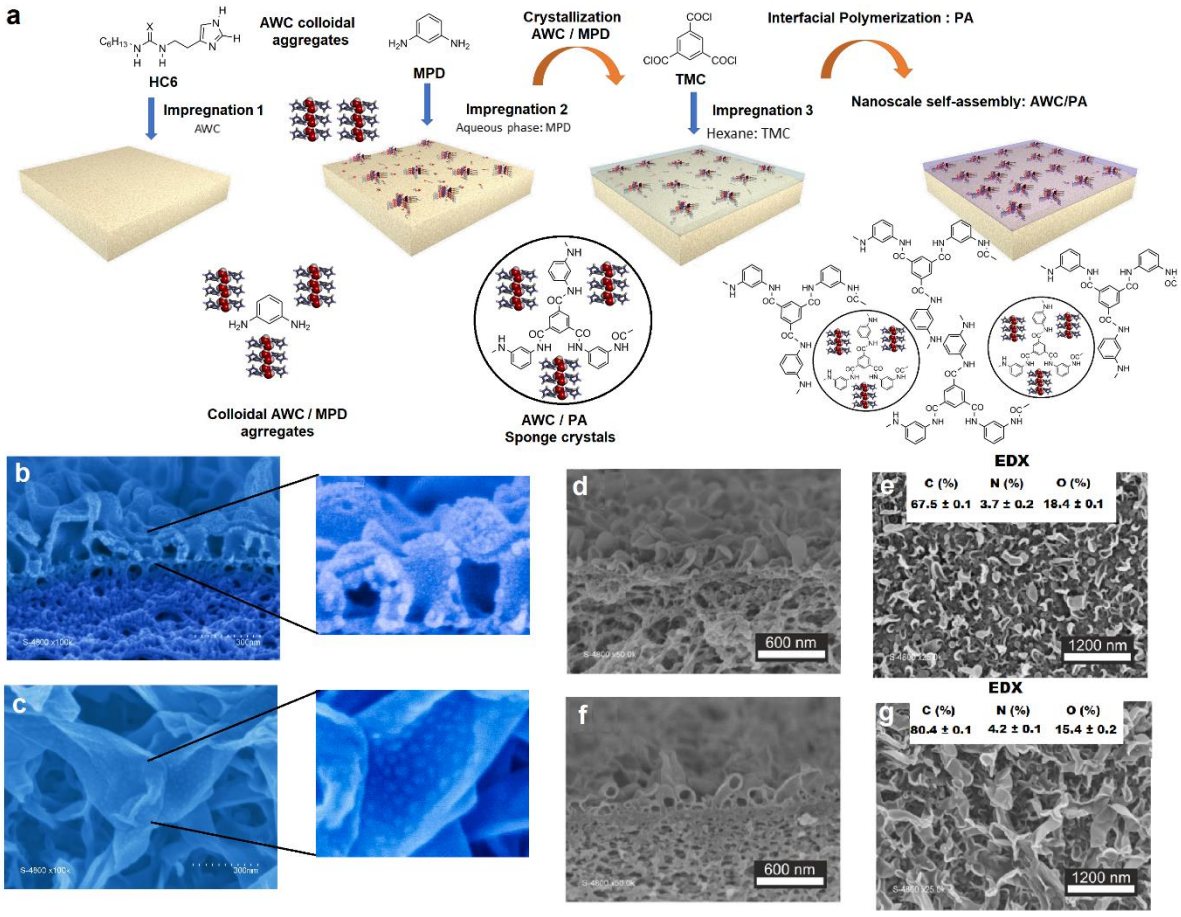

Fig. 1 | Membrane preparation and Scanning Electron Microscopy (SEM) characterization; **(a)** synthetic procedure to obtain the biomimetic TFC-HC6 membrane and hypothetical mechanism: impregnation 1 of the PSf ultrafiltration support with an aqueous/ethanolic solution of HC6, followed by the impregnation 2 with an aqueous solution of m-phenylenediamine (MPD) monomer and then the impregnation 3 with a hexane solution of trimesoyl chloride (TMC) monomer to begin to the IP and obtain the composite polyamide (PA) TFC-HC6 membranes incorporating AWCs. Representative SEM micrographs of **(b)** cross-sectional and **(c)** top view of the uppermost layer of TFC-HC6 films. SEM micrographs of **(d, f)** (left) cross-sectional and **(e,g)** of the surface showing compact structures of control TFC membranes **(d,e)** and the formation of large voids at the psf/PA interface of TFC-HC6 membranes **(f,g).** The elemental analysis was performed for each membrane by using energy dispersive X-ray spectroscopy (EDX).

The match between the distances of the ordered rows observed in the TEM micrograph and the periodicity of lamellar sheets in X-ray single crystal structure, indicates that the nanoparticles have a crystalline layered arrangement of I-quartets. We hypothesize that this phenomenon occurs in the first step of membrane synthesis, when the solution is poured on the surface of the PSf support. Subsequently, the IP procedure entails the contact of the support with an aqueous solution of MPD and aggregated phases of AWC/MPD are formed. Specifically, a heterogeneous nucleation is

promoted by H-bonding between MPD and colloidal AWC, as shown by DLS analysis. We did not observed a massive crystallization process, suggesting that this colloidal solution does not form an solid interlayer, as previously observed for other solid CNTS, GO, or MOFs fillers[28]. Then, the membrane is immersed in the TMC hexane solution, where the IP between MPD and TMC occurs roughly 10 seconds at the organic phase side of the interface. In this step, the diffusion of the pre-formed AWC/MPD colloids to the organic phase is disfavored, compared with the diffusion of MPD molecules, but they may interact with growing PA segments *via* H-bonding. This process results in the formation of cross-linked hybrid AWC-PA nanoparticles. They are embedded into the incipient PA layer formed on top and surrounding the nanoparticles. The new type of hybrid material is therefore generated *via* a nucleation/IP mechanism, supported by experimental results reported here. Scanning electronic microscopy (SEM) show the presence of the sponge-like nanoparticles, incorporated within the PA layer of TFC-HC6 membranes (Fig. 1b,c), while they are not observed for pristine membrane TFC. The close inspection of the SEM cross-sections and membrane surfaces (Fig. 1e,g) reveals a typical ridge-and-valley surface morphology[28-31]. However, the features observed with the incorporation of AWC are clearly larger than those of the pristine TFC membrane (Fig. 2d,e). This is also confirmed by atomic force microscopy (AFM) results (Supplementary Fig. 5). The TEM microscopy confirmed that, compared to reference pristine TFC layers (Fig. 2a), which have an homogeneous thickness of ~250 nm, the TFC-HC6 layers (Fig. 2b) have alternated thinner layers (~250 nm) and thicker (~500 nm) regions, a morphology that might also contribute to a higher surface area. It is also clear that we have a complex internal structure when the AWC are added, with differentiated domains in the TFC-HC6 layers. The AWC/PA nanoparticles, corresponding to the internal brighter spots with a lower electron density observed by TEM (Fig S7b-d), have diameter ~20-40 nm and are homogeneously enclosed (30-40 spots/100 μm^2) within the PA (Fig. 2b). The PA layer was preferentially stained with OsO_4 or RuO_4, to improve the contrast of the PA regions distributed around the brighter spots, that appears darker/grey in the TEM images of TFC (Fig. 2a)

and TFC-HC6 membranes (Fig. 2b). These areas are also clearly visible in the RuO_4 stained 2D (Supplementary Fig.7) and tomography (Supplementary Fig. 8) TEM images.

The presence of AWC is corroborated by results obtained with attenuated total reflectance (ATR)-Fourier transform infrared (FTIR) (Supplementary Figure 10) and energy dispersive X-ray (EDX) (Fig. 1e,g, Supplementary Table 3) spectroscopies: a) in addition to the vibrational bands of the PA of the TFC membrane, FTIR spectra of TFC-HC6 contain the $-CH_2-_{,as}$ and $-CH_2-_{,sym}$ stretches in the range 2750 – 2957 cm^{-1}, as well as urea-NHC=O and imidazole stretches at 1612 cm^{-1} and 1579 cm^{-1}, suggesting the incorporation of the HC6 within PA; b) the sharp band at 3300 cm^{-1} attributed to the O-H stretching vibration of strongly H-bonded water within I-quartets became much broader, reminiscent of the presence of more mobile water within the hybrid TFC-HC6 membrane; c) the elemental composition determined by EDX varied when AWC were incorporated in the PA, exhibiting a trend with up to 10-12% higher fraction of % C for TFC-HC6 layers and a concurrent reduction in % O.

The complexity of the structure can be clearly seen in the 3D TEM tomography movies (Supplementary Figure 8) or as screen shots of the 100-nm slices while tilting them at different angles (Fig. 2c), showing that larger voids and bright spots can be observed inside the TFC-HC6 when compared with the pristine TFC micrographs (Supplementary Fig. 7a and 8a), where very few or no bright spots are seen. The PSf support has much less contrast, appearing as light gray areas in the regular TEM (below the yellow line in Fig. 2a), while the PA layer formed on the surface of the PSf porous support is clearly darker. In the tomography in Fig. 2d, the position of the interface between the PSf support and the formed PA layer (green in Fig. 2d) is represented by a dash line. The less dense white grey spots that are hypothesized to be mostly composed by AWC/PA nanoparticles are marked purple in Fig. 2d. The relative volume occupied by the bright (purple in Fig. 2d) spots was estimated to be 20% by conducting the segmentation and calculating the total voxel of the purple zones relative to the total volume occupied by the complete PA/AWC layer.

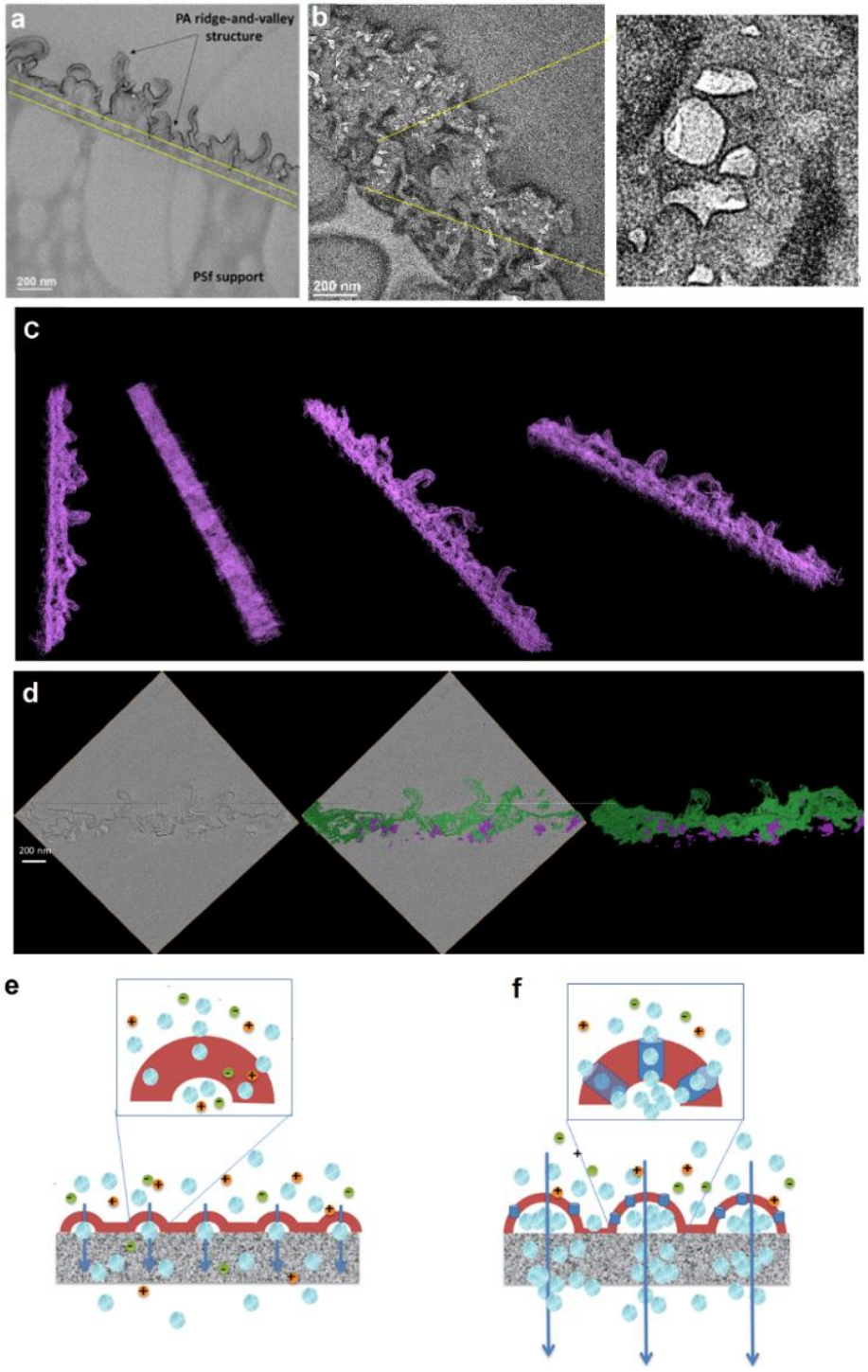

Fig. 2 | Morphological TEM characterization of the membranes. TEM cross-sectional images of **(a)** the pristine PA on porous PSf support and **(b)** detail of the top layer of the TFC-HC6 membrane with high magnification (membranes stained with OsO_4). **(c)** 3D reconstruction TEM tomography of TFC-HC6 membrane in different tilting angles. **(d)** Instantaneous screen shots of TFC-HC6 membrane tomography at a fixed angle: the PA layer formed on the surface of the PSf porous support (not visible) is marked in green. The less dense grey brighter spots, which could correspond to the AWC/PA nanoparticles are marked purple and represent an occupied relative volume of 20%. Schematic representation of the selective transport of water (blue spheres) *versus* ions (green and red spheres) across **(e)** compact pristine TFC and (**f**) AWC-embedded TFC-HC6 membranes with larger surface area.

Desalination performances and stability under RO conditions

The free-defect distribution of sponge-like PA-AWC regions are essential to increase their performance, since they determine the pathways for the water flow across the active film (Fig. 2e,f). For the first time, biomimetic membranes were tested under high-pressure crossflow conditions, representative of seawater desalination operations in real plants. Specifically, optimized TFC-HC6 layers comprising AWC provided a consistent increase in water flux of roughly 75% and 150% in the desalination of mimicked seawater (Fig. 3a) and brackish water (Fig. 3d), respectively, compared to lab-made control TFC membranes.

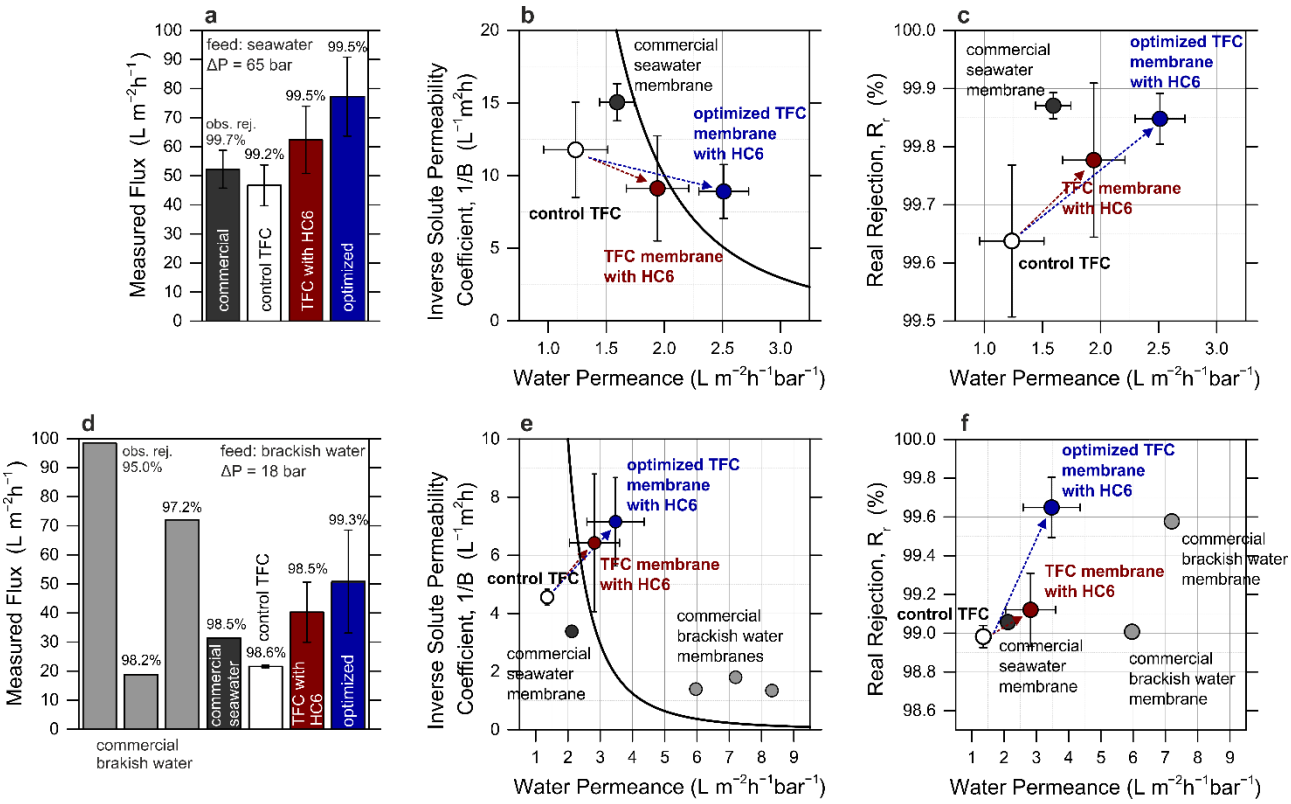

Fig. 3 | Performance of the membranes in the desalination of **(a-c)** seawater and **(d-f)** brackish water. (**a**, **d**) Experimental water flux and observed solute rejection of control TFC membranes, commercial membranes, and TFC-HC6 membranes incorporating AWCs at 0% recovery. The filtration conditions were: 65 bar applied pressure with 35000 ppm NaCl feed solution at pH 8 for seawater desalination; 18 bar applied pressure with 5800 ppm NaCl feed solution at pH 7 for brackish water desalination. **(b, e)** Selectivity-productivity trade-off graphs plotting the inverse solute permeability coefficient of the membranes as a function of their respective water permeance; the solid line depicts the proposed TFC upper bound relationship. (**c**, **f**) Calculated real rejection of the membranes as a function of respective water permeance. The feed solution temperature in all the tests was 27±1 °C.

This notable productivity was achieved while maintaining or, in many instances, while improving the observed NaCl solute rejection to ~ 99.5%, relative to traditional TFC membranes. Our membranes also displayed a better combination of productivity and selectivity compared to marketed state-of-the-art membranes, which were tested in the lab under analogous conditions. Please note that an increase in the solute permeability coefficient *(B*) is commonly expected when the water permeance (*A*) increases, as *B* represents the flux of solutes dissolved in the permeating water: thus, as water flux increases, the solute flux is also higher at equivalent values of solute rejection.

However, in this study, higher water permeance was obtained with little increase, or even with a decrease of solute permeability coefficient. This phenomenon is explained with the concurrent increase of both water flux and solute rejection (Fig. 3b,c,e,f). A conventional and robust method to compare different membranes is to plot their performance in a permeability-selectivity trade-off chart (Fig. 3b,e). While the data associated with lab-made control membranes are placed below the upper bound, mostly due to low water permeance, the membranes incorporating AWCs defeat the trade-off. This result is especially true for optimized TFC-HC6 membranes, whose permeability-selectivity performance places them well beyond the bound line. The improvements accomplished with the incorporation of AWCs are especially evident when the real rejection provided in desalination experiments is plotted against the water permeance (Fig. 3c,f). Real rejection is evaluated taking into account concentration polarization phenomena that occurred during filtrations and is a better parameter than observed rejection to understand the intrinsic selectivity of the membranes. To assess the performance of the membranes with real seawater, low-recovery experiments were also performed using the recipe for substitute ocean water of the ASTM D1141-98 (2013) as feed solution. A water flux of 66.8 ± 3.8 LMH was obtained, with an observed conductivity rejection of 99.4 ± 0.1 %, and an observed boron rejection of 91.2 ± 1.5%. Details on the experimental conditions, on the ionic composition of the feed and permeate samples, as well as for values of observed rejection of individual ions are presented in Supplementary Table 8.

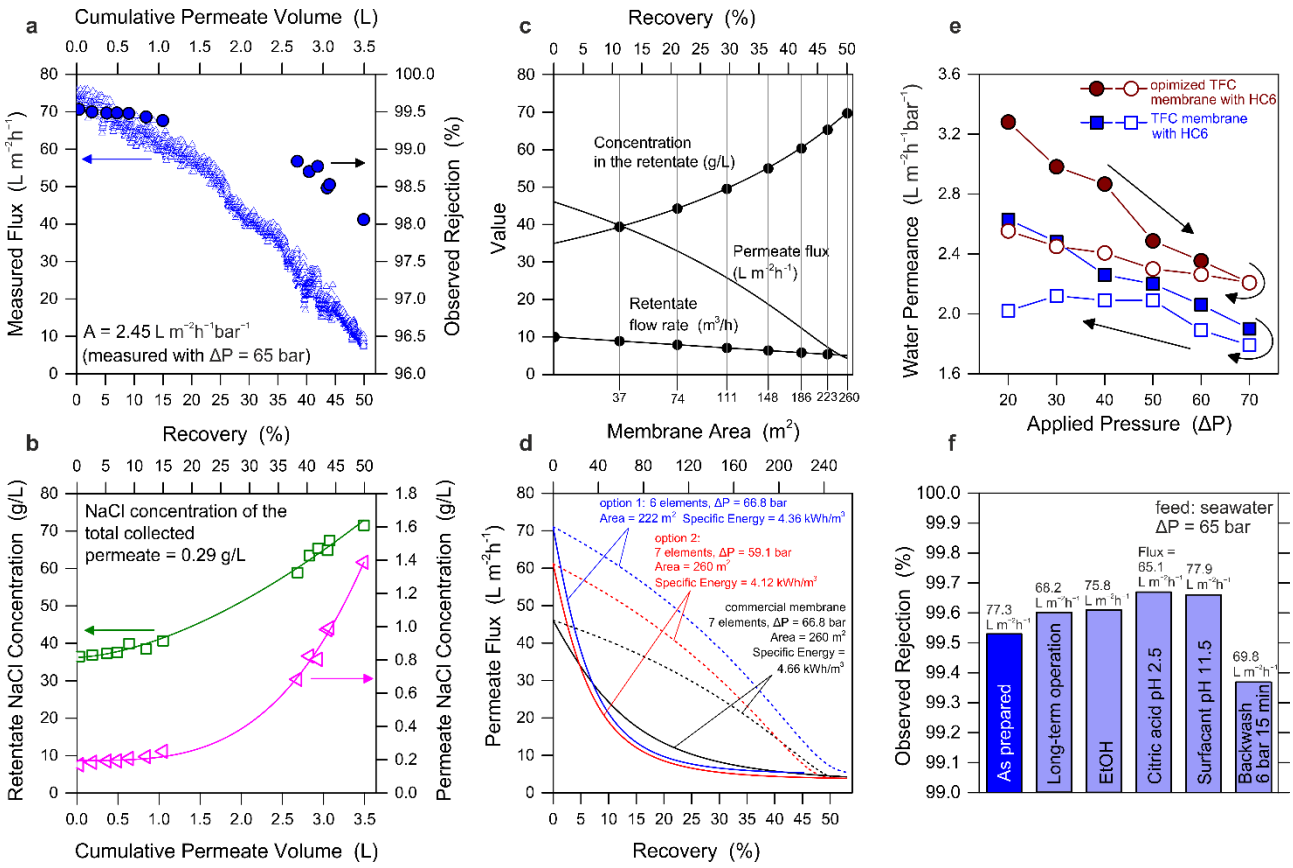

Fig. 4 | Application of the membranes in typical seawater desalination operation. (a, b) Experimental water flux, observed solute rejection, feed and permeate stream concentrations as a function of recovery and cumulative permeate volume; here, the filtration conditions were: 65 bar applied pressure with 35,000 ppm NaCl feed solution at pH 8 and a final recovery of 50%. **(c)** Validation of the vessel-scale model for SW30XHR commercial membranes and **(d)** outcome of the application of the model for the commercial membranes and for the TFC-HC6 membranes incorporating AWCs; here, the profile of permeate flux within the vessel is plotted as a function of (solid lines) space, i.e., cumulative membrane area, or (dash lines) recovery rate. **(e)** Experimental water permeance in tests comprising a stepwise increase followed by a stepwise decrease of applied pressure. **(f)** Experimental performance of membranes subjected to mechanical or chemical stress; here, the filtration conditions were: 65 bar applied pressure with 35,000 ppm NaCl feed solution at pH 8 and recovery of 0%.

The membranes TFC-HC6 incorporating AWCs were further assessed when applied in high-recovery filtration, as in commercial desalination processes. Experiments were conducted by achieving 50% recovery of freshwater from a synthetic feed approximating the salinity and the pH of typical seawater. The data in Fig. 4a,b, show the trend of permeate flux as a function of recovery: the flux profile decreases steadily from the initial value of 75 L m^{-2} h^{-1} due to the reduction in driving force as the feed solution was increasingly concentrated. The average water flux of the test was 34.4 L m^{-2} h^{-1} and the concentration of the product water was 290 mg/L, a value related to an excellent

palatability based on the WHO Guidelines for Drinking-Water Quality. This experiment approaches the flux profile and the solute concentrations that would be obtained inside a pressure vessel of a full-scale system for a single pass sweater RO process, and it confirms the promising performances of the TFC-HC6 membranes under representative full-scale conditions. We surmise that the enhanced fluid dynamics of real membrane elements would further reduce the effect of concentration polarization when compared with lab-scale experiments, thus realizing even larger water fluxes and a higher permeate quality. Therefore, a vessel-scale model was implemented to compute the membrane area and the energy required to extract high-quality water from a feed of seawater, by applying current commercial RO membranes and the bioinspired membranes proposed in this work.

As shown in Fig. 4c, the vessel-scale model, represented by solid lines, was first validated with high-rejection SW30XHR-400i DuPont elements, against the results provided by the software Wave (DuPont) and plotted as black dots. The model accurately described the profile of flux and concentration within the system. Once validated, the model was thus applied in two optional implementations of our bioinspired membranes (Fig. 4d). The modeling outcome suggests that, if the same pressure of 66.8 bar is applied in the vessel, 50%-recovery desalination may be achieved with six instead of seven elements in series, which are instead needed when applying current commercial seawater desalination membranes. In other words, the larger permeance of the membrane TFC-HC6 incorporating AWCs would allow the use of a smaller membrane area, translating in near proportional savings in capital and membrane replacement costs, with also a reduction of the specific energy from 4.66 to 4.36 kWh for each m^3 of product freshwater. A possibly more advantageous configuration would involve the same number of elements with respect to current commercial membranes, that is, identical membrane area and capital costs, but a lower applied pressure of 59.1 bar. According to the model, this arrangement would provide a more uniform permeate flux within the vessel and a noteworthy 12% reduction of the required energy to produce the same amount of freshwater. It is important to highlight that the application of membrane elements is subject to several constraints in

terms of minimum and maximum cross-flow rate, maximum permeate flux, as well as maximum recovery rate, which can only be evaluated at the time of full-scale system design.

A final set of experiments were conducted to understand the resilience of the layers to mechanical and chemical stress. The materials displayed a partially plastic behavior, as membranes could not entirely recover their original permeance once subjected to high hydraulic pressures (Fig. 4e). Nevertheless, the novel membranes were notably robust and maintained their selectivity after being subject to mechanical solicitations, including changes in pressure, to backwash, and in long-term filtration experiments. The transport performance of the bioinspired membranes was also unaffected by exposure to relatively harsh environments representative of real systems, where membranes would undergo cycles of physical and chemical cleaning, often with the use of acidic, basic, and/or amphiphilic compounds. The results in Fig. 4f indicate that similar or higher NaCl rejection than pristine membranes was observed after these were exposed to solutions of different chemistry. Perhaps the most significant outcome is related to the ability of the materials to maintain high performance following immersion in pure ethanol, which was used during HC6 synthesis and to solubilize this compound during membrane fabrication. This result suggests that the AWCs were effectively incorporated within the PA matrix and no detrimental effects of leaching or re-solubilization were detected, as the membranes showed no loss in performances (Fig. 4f).

Conclusions

This rationalization corroborates the results discussed above, suggesting that the embedded self-assembled AWCs did not generate defects of the uppermost active layer. Indeed, the highly selective AWC are intrinsically promoting the preferential selective passage of water with a significantly better perm-selective behavior through a selective AWC embedded layer with larger surface area. It also implies an excellent structural compatibility of AWCs with the surrounding PA matrix, a necessary requisite to construct a seamless active layer without defects.

References

1. Mekonnen, M. M. & Hoekstra, A. Y. Four billion people facing severe water scarcity. *Sci. Adv.* **2,** e1500323 (2016).
2. Eliasson, J. The rising pressure of global water shortages. *Nature* **517,** 6–7 (2015).
3. Shannon, M. A. *et al.* Science and technology for water purification in the coming decades. *Nature* **452**, 301–310 (2008).
4. Cadotte, J. E., Petersen, R. J., Larson, R. E. & Erickson, E. E. A new thin-film composite seawater reverse osmosis membrane. *Desalination* **32**, 25–31 (1980).
5. Karan, S., Jiang, Z. & Livingston, A. G. Sub-10 nm polyamide nanofilms with ultrafast solvent transport for molecular separation. *Science* **348**, 1347–1351 (2015).
6. Chowdhury, M. R., Steffes, J., Huey, B. D. & McCutcheon, J. R. 3D printed polyamide membranes for desalination. *Science* **361**, 682–686 (2018).
7. Tan, Z., Chen, S., Peng, X., Zhang, L. & Gao, C. Polyamide membranes with nanoscale Turing structures for water purification. *Science* **360**, 518–521 (2018).
8. Jeong, B. H. *et al.* Interfacial polymerization of thin film nanocomposites: A new concept for reverse osmosis membranes. *J. Memb. Sci.* **294**, 1–7 (2007).
9. Duan, J. *et al.* High-performance polyamide thin-film-nanocomposite reverse osmosis membranes containing hydrophobic zeolitic imidazolate framework-8. *J. Memb. Sci.* **476**, 303–310 (2015).
10. Ratto, T. V, Holt, J. K. & Szmodis, A. W. Asymmetric nanotube containing membranes. *U.S.* US Patent 7993524 (2011).
11. Werber, J. R., Deshmukh, A. & Elimelech, M. The Critical Need for Increased Selectivity, Not Increased Water Permeability, for Desalination Membranes. *Environ. Sci. Techol. Lett.* **3**, 112–120 (2016).
12. Agre, P. Aquaporin water channels (Nobel lecture). *Angew. Chem. Int. Ed.* **43**, 4278–4290

(2004).

13. Eriksson, U. K. *et al.* Subangstrom resolution x-ray structure details aquaporin-water interactions. *Science* **340**, 1346–1349 (2013).

14. Tang, C. Y., Zhao, Y., Wang, R., Hélix-Nielsen, C. & Fane, A. G. Desalination by biomimetic aquaporin membranes: Review of status and prospects. *Desalination* **308**, 34–40 (2013).

15. Barboiu, M. Artificial water channels. *Angew. Chem. Int. Ed.* **51**, 11674–11676 (2012).

16. Barboiu, M. & Gilles, A. From natural to bioassisted and biomimetic artificial water channel systems. *Acc. Chem. Res.* **46**, 2814–2823 (2013).

17. Leduc, Y. *et al.* Imidazole-quartet water and proton dipolar channels. *Angew. Chem. Int. Ed.* **50**, 11366–11372 (2011).

18. Hu, X. B., Chen, Z., Tang, G., Hou, J. L. & Li, Z. T. Single-molecular artificial transmembrane water channels. *J. Am. Chem. Soc.* **134**, 8384–8387 (2012).

19. Si, W. *et al.* Selective artificial transmembrane channels for protons by formation of water wires. *Angew. Chem. Int. Ed.* **50**, 12564–12568 (2011).

20. Licsandru, E. *et al.* Salt-Excluding Artificial Water Channels Exhibiting Enhanced Dipolar Water and Proton Translocation. *J. Am. Chem. Soc.* **138**, 5403–5409 (2016).

21. Tunuguntla, R. H. *et al.* Enhanced water permeability and tunable ion selectivity in subnanometer carbon nanotube porins. *Science* **357**, 792–796 (2017).

22. Kocsis, I. *et al.* Oriented chiral water wires in artificial transmembrane channels. *Sci. Adv.* **4**, (2018).

23. Werber, J. R. & Elimelech, M. Permselectivity limits of biomimetic desalination membranes. *Sci. Adv.* **4**, eaar8266 (2018).

24. McGinnis, R. L. *et al.* Large-scale polymeric carbon nanotube membranes with sub-1.27-nm pores. *Sci. Adv.* **4**, e1700938 (2018).

25. Mi, B. Graphene oxide membranes for ionic and molecular sieving. *Science* **343**, 740–742

(2014).

26. Yang, Y. *et al.* Large-area graphene-nanomesh/ carbon-nanotube hybrid membranes for ionic and molecular nanofiltration. *Science* **364**, 1057–1062 (2019).

27. Shen, Y. X. *et al.* Achieving high permeability and enhanced selectivity for Angstrom-scale separations using artificial water channel membranes. *Nat. Commun.* **9**, 2294 (2018).

28. Lin, L., Lopez, R., Ramon, G. Z. & Coronell, O. Investigating the void structure of the polyamide active layers of thin-film composite membranes. *J. Memb. Sci.* **497**, 365–376 (2016).

29. Pacheco, F., Sougrat, R., Reinhard, M., Leckie, J. O. & Pinnau, I. 3D visualization of the internal nanostructure of polyamide thin films in RO membranes. *J. Memb. Sci.* **501**, 33–44 (2016).

30. Wong, M. C. Y., Lin, L., Coronell, O., Hoek, E. M. V. & Ramon, G. Z. Impact of liquid-filled voids within the active layer on transport through thin-film composite membranes. *J. Memb. Sci.* **500**, 124–135 (2016).

31. Li, Y. *et al.* Probing flow activity in polyamide layer of reverse osmosis membrane with nanoparticle tracers. *J. Memb. Sci.* **534**, 9–17 (2017).

Data availability

The data that support the findings of this study are available from the corresponding author (Mihail Barboiu) on reasonable request.

Acknowledgements

This work was supported by Agence Nationale de la Recherche ANR-18-CE06-0004-02, WATERCHANNELS and ERANETMED2-72-357 IDEA
. The authors thank Didier Cot (University of Montpellier) for SEM experiments, Francesco Ricceri (Politecnico di Torino) for help with filtration experiments and Mihai Deleanu (University of Montpellier) for help with the organic synthesis of HC6 and characterization.

Author Contributions M.B. conceived the project and designed the experiments. M.Di V. fabricated the membranes, performed IR, EDX characterization and SEM analysis; L. H. performed XPRD analysis, M. Di V. and A. T. designed and performed the filtration experiments. S.N. designed and V.M., S.C., R.S., performed DLS, SAXS and TEM experiments and conducted the experimental analysis. M.B. wrote the manuscript with input from all authors. All authors discussed the results and commented on the manuscript

Competing interests

M.B. M. DV. A.T. are inventors on a provisional patent application submitted in 2019 by the SATT AxLR on behalf of the Centre National de la Recherche Scientifique -CNRS for the design, synthesis and performances of the membrane materials in this study.

Additional information

Supplementary Information is available in the online version of the paper.

Correspondence and requests for materials should be addressed to M.B.

Reprints and permission information is available online at www.nature.com/reprints.